

Detecting Beam Blockage in Radar-Based Precipitation Estimates

D. BRENT MCROBERTS

*Department of Geography, and Department of Atmospheric Sciences, Texas A&M University,
College Station, Texas*

JOHN W. NIELSEN-GAMMON

Department of Atmospheric Sciences, Texas A&M University, College Station, Texas

(Manuscript received 9 September 2016, in final form 5 April 2017)

ABSTRACT

Gridded radar-based quantitative precipitation estimates (QPEs) are potentially ideal inputs for hydrological modeling and monitoring because of their high spatiotemporal resolution. Beam blockage is a common type of bias in radar QPEs related to the blockage of the radar beam by an obstruction, such as topography or tall buildings. This leads to a diminishment in the power of the transmitted beam beyond the range of obstruction and a systematic underestimation of reflectivity return to the radar site. A new spatial analysis technique for objectively identifying regions in which precipitation estimates are contaminated by beam blockage was developed. The methodology requires only a long-term precipitation climatology with no prerequisite knowledge of topography or known obstructions needed. For each radar domain, the QPEs are normalized by climatology and a low-pass Fourier series fit captures the expected precipitation as a function of azimuth angle. Beam blockage signatures are identified as radially coherent regions with normalized values that are systematically lower than the Fourier fit. Precipitation estimates sufficiently affected by beam blockage can be replaced by values estimated using neighboring unblocked estimates. The methodology is applied to the correction of the National Weather Service radar-based QPE dataset, whose estimates originate from the NEXRAD network in the central and eastern United States. The methodology is flexible enough to be useful for most radar installations and geographical regions with at least a few years of data.

1. Introduction

Over the past decade, hydrological monitoring and modeling has been greatly enhanced with the increased availability of high-resolution gridded precipitation datasets. Gridded radar-based precipitation estimates are available at high resolution with very low-latency times and form the core of such rainfall analyses as the National Weather Service's Stage IV precipitation analysis (Lin and Mitchell 2005) in areas of good radar coverage. Radar-based precipitation estimates typically provide better spatiotemporal resolution of precipitation than other measurement systems or retrievals.

One downside is that radar estimates often contain biases due to the spatial differences in the sampling properties of a radar beam. In normal operations, the vertical sampling of the hydrometeor profile is limited to a

fixed set of tilt angles whose altitude above ground level and above radar height is range dependent. This leads to a spatial heterogeneity of radar estimates related to the distance of the beam from the radar site that produces range-dependent biases. Numerous correction algorithms having been developed to deal with such biases (e.g., Andrieu and Creutin 1995; Vignal et al. 1999; Vignal and Krajewski 2001; Zhang et al. 2008; Krajewski et al. 2011), often relying on the vertical profile of reflectivity (VPR).

Another well-understood type of bias and the focus of this paper is beam blockage, which can be defined as a sudden interception of a transmitted radar beam, in most cases by a fixed nonmeteorological obstruction, such as a tall building or terrain feature (Smith 1998; Krajewski et al. 2006). For obstructions near the radar site, the effects of the beam blockage in precipitation estimation can be minimized through the use of higher, unblocked beams. When this is the case, regions at some distance beyond the obstruction where estimates are derived from the lower, blocked beams will be contaminated by beam blockage.

Corresponding author: D. Brent McRoberts, mcrobert@tamu.edu

DOI: 10.1175/JTECH-D-16-0174.1

© 2017 American Meteorological Society. For information regarding reuse of this content and general copyright information, consult the [AMS Copyright Policy](http://www.ametsoc.org/PUBSReuseLicenses) (www.ametsoc.org/PUBSReuseLicenses).

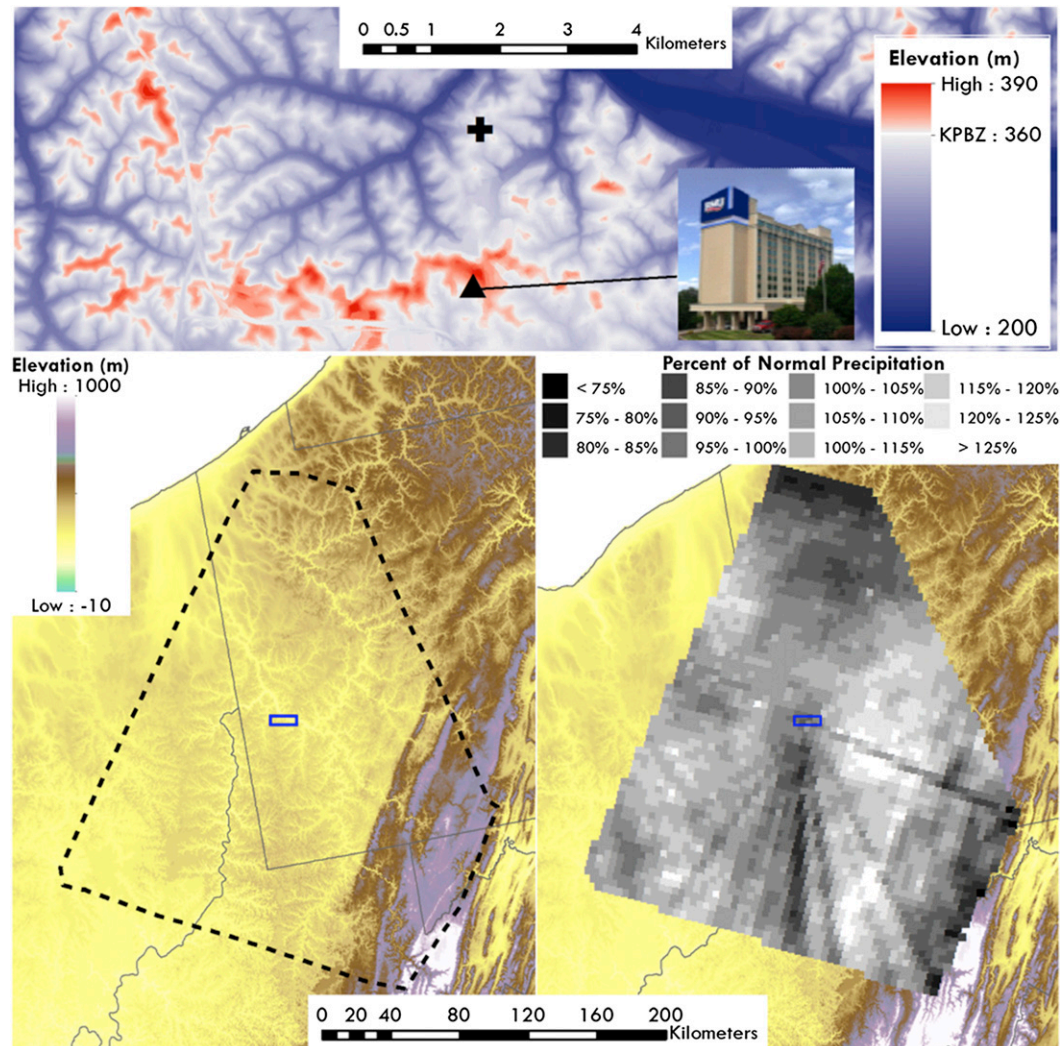


FIG. 1. (top) Elevation with a color legend relative to the KPBBZ radar site (+) and the location of Yorktown Hall (▲). (bottom left) KPBBZ effective radar coverage area (dotted line), and (bottom right) 36-month PNP.

Hydrometeors beyond the location of beam interception are systematically unsampled or are sampled by a reduced-power beam. A reduction in the transmitted beam causes a diminished return beam, a low-biased reflectivity value, and a low-biased estimation of precipitation through application of a reflectivity–rainfall (Z – R) relationship (Joss and Waldvogel 1990; Smith 1998; Bech et al. 2003). In mountainous regions beam blockage is nearly impossible to escape (Joss and Waldvogel 1990), and in these regions gridded precipitation estimates usually rely on other sources (Krajewski et al. 2010; Zhang et al. 2013), even if the radar is installed at a peak in the topography (Joss and Lee 1995).

An example of a region affected by beam blockage is south of the Pittsburgh, Pennsylvania (KPBBZ), radar (Fig. 1, bottom left). The Alleghany Mountains run through

the southeastern portion of the radar-effective coverage area, with some evidence of this topography leading to lower reflectivity returns. Of greater interest is the topography in the immediate vicinity of the KPBBZ radar site. Beams traveling southward encounter buildings on terrain that are 30 m in elevation higher than the radar site within 2 km of transmission (Fig. 1, top). A significant obstruction is the 11-story-tall Yorktown Hall near the campus of Robert Morris University (Fig. 1, top), a building that was constructed in 1972 on ground that is more than 10 m in elevation higher than the KPBBZ radar site. The reduction in transmitted beam power beyond a few kilometers south of the radar site is clearly evident (Fig. 1, bottom right).

Most recent approaches for correcting beam blockage in the United States have utilized dual-polarization radar parameters, which are now widely available after

recent upgrades to the Next Generation Weather Radar (NEXRAD, also known as WSR-88D) network (Istok et al. 2009). Use of the specific differential phase (K_{DP}) parameter has been common because of its insensitivity to beam blockage relative to Z (e.g., Cifelli et al. 2002; Friedrich et al. 2007; Lang et al. 2009; Zhang et al. 2013). Specific attenuation A is another parameter insensitive to blockage and relies less on the drop size distribution than K_{DP} (Ryzhkov et al. 2014; Diederich et al. 2015).

Another approach has been to use digital elevation models (DEMs) to identify topographical related blockages (e.g., Andrieu et al. 1997; Kucera et al. 2004; Krajewski et al. 2006; Lang et al. 2009). Techniques for correcting estimates in regions affected by blockages have utilized the VPR (e.g., Germann et al. 2006; Tabary 2007).

All of these approaches use information available in real time and knowable to the radar operators. However, gridded precipitation estimates are several steps removed from the suite of radar data collected at individual sites. While individual beam blockage corrections may have been applied prior to precipitation estimation, such corrections are difficult because of the low signal-to-noise ratios of partial beam blockages. Also, while on-site near-real-time beam blockage correction algorithms may continue to improve, there is a need for correction of beam blockage in archived precipitation analyses for purposes such as input to land surface models for development of soil moisture climatology.

In this paper, we describe and validate an objective algorithm to detect regions of beam blockage in Cartesian-gridded radar-based precipitation estimates. Unlike previous approaches to detect beam blockage, this algorithm operates directly on precipitation estimates rather than reflectivity or other such radar data. We assume that beam blockage obstructions are fixed in time and apply the algorithm to accumulated precipitation estimates over 36-month periods, enhancing the signal-to-noise ratio over single-volume-scan information.

This paper is one of a set of three for detection and correction of long-term precipitation estimates. Another discusses methods for detecting and correcting for range-dependent biases (using data that are adjusted by the methods of this paper). The third describes a two-dimensional Kriging procedure to detect biases not characterized as beam blockage or range dependent. The complete set of papers describes a comprehensive algorithm for reduction of errors in radar-based precipitation estimates.

2. Data

This study uses the daily National Weather Service (NWS) quantitative precipitation estimates (QPEs),

which are gridded precipitation analyses covering the continental United States (CONUS) and which represent a subjective merging of radar-, gauge-, and satellite-based precipitation estimates (Lin and Mitchell 2005). Our study region avoids the western CONUS (Fig. 2), where the QPEs rely more heavily on gauges and digital elevation models (Zhang et al. 2013). The NWS QPE grids use the Hydrologic Rainfall Analysis Project (HRAP) coordinate system, a polar stereographic projection with a roughly 4-km spatial resolution (Fulton 1998). The NWS QPEs, which we obtained from online (water.weather.gov/precip/p_download_new), are temporally complete since 1 January 2005. In this study, daily QPE data were aggregated to 36-month totals and were converted to percent of normal precipitation (PNP) using the Parameter-Elevation Regressions on Independent Slopes Model (PRISM) 1981–2010 climate normals (Daly et al. 1994), which are also available on the HRAP grid. The same PRISM normals values were used to normalize gauge observations for algorithm validation.

3. Algorithm

a. Overview

Beam blockage is most naturally described using radar-centric polar coordinates, with the horizontal coordinates being distance and azimuth. Here we follow the convention of azimuth values beginning at zero in the northward direction and increasing clockwise. The term *radial* will refer to a straight line extending from the radar site to the edge of a radar domain. Beam blockage is manifested as an underestimation of precipitation that is azimuthally bounded and limited to locations beyond the radius of the blockage. This underestimation due to blockage should be radially consistent beyond an obstruction in regions with a single blockage feature, though other effects such as beam broadening and overshooting can complicate this assumption in the cases of partial blockage. Therefore, our algorithm emphasizes methods for minimizing spurious blockage related to range-related radar effects.

The four major steps in the algorithm are as follows:

- 1) Determine the location of QPE grid cells in radar-centric polar coordinates.
- 2) Find and flag grid cells with apparent azimuthally bounded precipitation underestimates.
- 3) Identify blocked regions using flagged grid cells forming contiguous radially consistent precipitation underestimates.
- 4) Identify the apparent location of the blockage.

Once the QPE grid cells subject to beam blockage have been identified, the precipitation estimates within

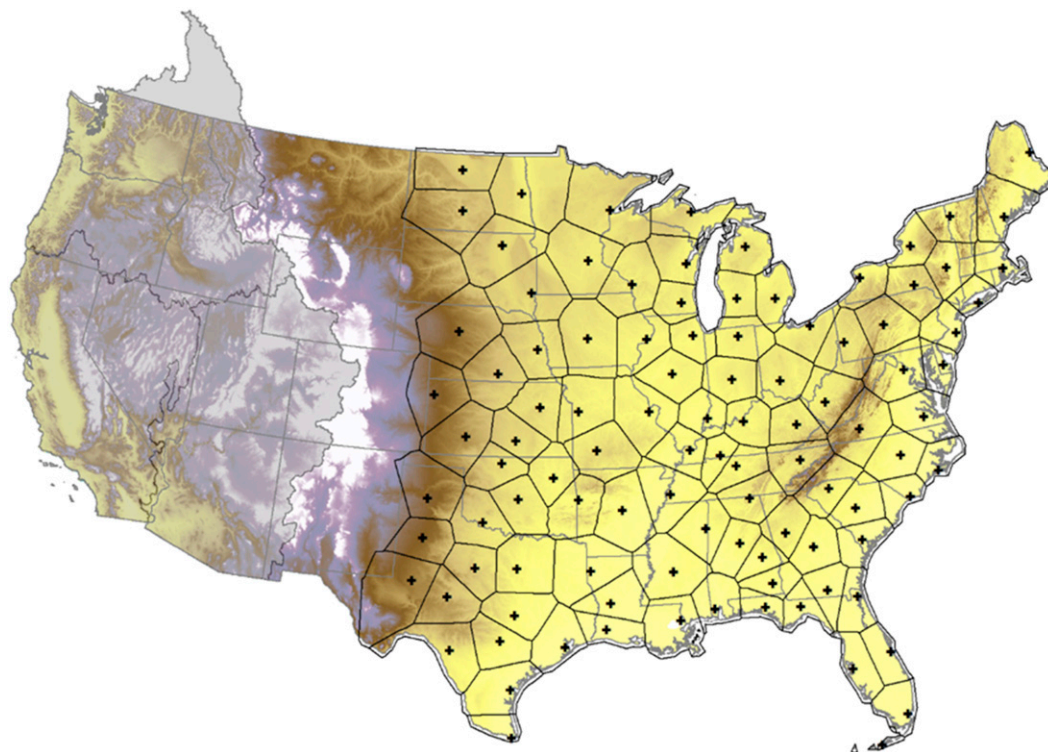


FIG. 2. Location of the NEXRAD radar sites (small + signs) and coverage areas (black lines) in our study region. The area covered by the three River Forecast Centers (RFCs) in the western CONUS have gray shading.

those cells may simply be flagged as erroneous or adjusted using any convenient method. Section 5 describes a method that uses information collected during the blockage identification procedure to adjust precipitation totals in the flagged grid cells.

b. Locating grid cells within radar coverage areas

The NWS QPE dataset uses data from the NEXRAD network as the primary input. Therefore, we assigned each HRAP grid cell to a single NEXRAD site (Fig. 2), choosing the one that was the shortest geographical distance. There are more sophisticated techniques for delineating effective coverage areas (Breidenbach et al. 1999, 2001; Testik and Gebremichael 2010), but these require separate observations from multiple radars, which is not information included in the NWS QPE dataset. As blending of data from multiple radars to produce QPE-type analyses becomes more common, the algorithm can be modified to allow detection of apparent beam blockages whose blockage strength decreases with distance from the radar as data from other radars contribute to the analysis.

Each radar domain is mapped onto a two-dimensional polar coordinate grid (d, θ) using the radar site as the origin, d as the distance from the radar site, and θ as the

azimuth angle. The polar grid is segmented into non-overlapping annuli with a width of 10 km (e.g., Fig. 3) and nonoverlapping slices extending from the radar site to the edge of the radar domain (we call these azimuthal sectors) with a constant width of 1° ($0^\circ-1^\circ$, $1^\circ-2^\circ$, etc.). This azimuthal sector width corresponds to the half-power beamwidth of the NEXRAD radars (Fulton et al. 1998). Polar coordinates are computed for each grid cell (d_{GC}, θ_{GC}) using the latitude–longitude coordinates of the cell centroid and the radar site location. Each grid cell is assigned to the annulus into which its midpoint falls.

For this study, we devised a new quantity called the fraction of each grid cell [fraction of grid cell (FOG)] that falls within each azimuthal sector. FOG is computed by passing an arc through the gridcell centroid (d_{GC}, θ_{GC}), with a length that is the width of the grid cell. Each grid cell has a value $\text{FOG}(i, \theta)$ ranging from 0 to 1 for all 360 azimuthal sectors, such that

$$\sum_{\theta=0^\circ}^{359^\circ} \text{FOG}(i, \theta) = 1. \quad (1)$$

For example, if the arc used to compute FOG for grid cell i spans exactly the 0° and 1° azimuthal sectors (2° in width), then $\text{FOG}(i, 0^\circ) = 0.5$ and $\text{FOG}(i, 1^\circ) = 0.5$. For grid cells



FIG. 3. KGWX radar domain with the 10-km annuli surrounding the radar site (+ sign)

near the radar site, the arc will span several azimuthal sectors with FOG values closer to zero than to one.

c. Flagging HRAP grid cells with lower-than-expected precipitation

Many factors can cause radar-based precipitation estimates to be low, only one of which is beam blockage. For example, there may also be errors in the applicability of the $Z-R$ relationship, or range-dependent biases. Ground truth (gauge) data are generally not available at sufficient spatial resolution to identify the spatial signature of narrow beam blockages. Instead of comparing precipitation estimates to other data, the algorithm looks for the spatial signatures of beam blockage within the precipitation estimation pattern itself.

Grid points that are candidates for beam blockage are identified by comparison with other grid points within the same annulus. A smooth Fourier series function is fit to the PNP (as a function of azimuth angle) of all grid cells within an annulus. The Fourier series represents a function with a periodic signal as a summation of sine and cosine waves and is particularly useful for azimuthally dependent functions (Brandwood 2012). In our study, we compute the Fourier series fit \hat{P} as

$$\hat{P}(\theta) = \sum_{n=1}^k A_n \cos\left(\frac{2\pi n\theta}{360^\circ}\right) + B_n \sin\left(\frac{2\pi n\theta}{360^\circ}\right), \quad (2)$$

where A_n and B_n are coefficients for each wavenumber n ($\lambda = 360^\circ/n$) and k is the maximum wavenumber in the summation.

Given a departure of the PNP value P from the Fourier series fit \hat{P} , we compute the residual for each grid cell ($P - \hat{P}$). Grid points that are affected by beam blockage should have substantially lower PNP than the smooth function would predict. The grid cell i with the largest negative residual among all n grid cells is flagged as possibly beam blocked. We then determine how anomalous grid cell i is relative to the other grid cells within the same annulus. Grid cell i is flagged if the ratio R of the squared residual to the mean squared residual of all other grid cells, computed as

$$R(i) = \frac{[P(i) - \hat{P}(i)]^2}{\frac{1}{n-1} \sum_{j=1, j \neq i}^n [P(j) - \hat{P}(j)]^2}, \quad (3)$$

exceeds some threshold ratio value R_0 .

The process is then repeated for the same annulus, but with grid cell i excluded from the Fourier function fit. Additional grid cells are successively flagged as possibly beam blocked until there is no longer any grid cell whose $R(i)$ exceeds the threshold. In our study area, a value of $R_0 = 5.0$ sufficiently separated grid cells with lower-than-expected PNP from other grid cells (e.g., Fig. 4).

The Fourier fit should adequately capture the spatial variability of precipitation without overfitting the data. If k is too small, then natural spatial variability may be mistaken for lower-than-expected precipitation, and vice versa if k is too large. Various values of k were tested by checking the flagging of grid cells in radar domains that had clear visual evidence of beam blockage—for example, the performance of Fourier series fits for an annulus in the Columbus Air Force Base, Mississippi (KGWX), radar domain with clear visual evidence of beam blockage (Fig. 4). A low-wavenumber fit ($k = 3$) is effective at finding broader regions of negative residuals but is not as adept at finding slimmer regions (Fig. 4c). Conversely, the overfit of the higher wavenumber ($k = 24$) is better at finding slimmer regions of negative residuals but fails to identify broader regions of blocking (Fig. 4g). Overall, an intermediate wavenumber fit ($k = 12$) provides the most satisfactory solution to the flagging of grid cells in the KGWX domain and the others in our study region.

After the flagging procedure is completed for all annuli, a quantity called the gridcell blockage indicator b is computed at grid cell i as

$$b(i) = 1 - \frac{P(i)}{\hat{P}(i)}. \quad (4)$$

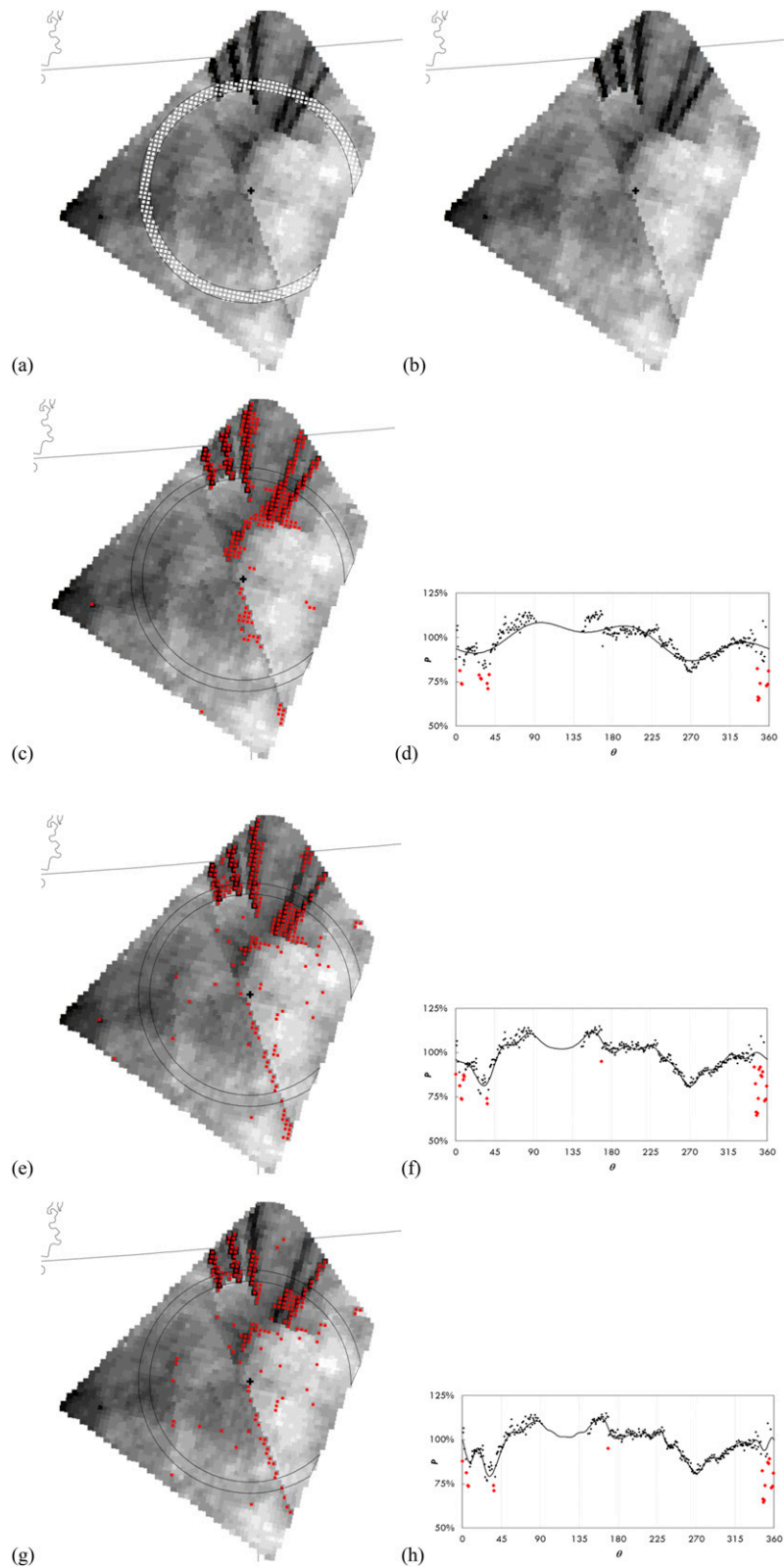


FIG. 4. KGWX radar domain. (a) Grid cells in the 90–100-km annulus and (b) P values (black: $P \leq 0.7$; white $P \geq 1.2$). (c) Grid cells flagged using $k = 3$ (red), and (d) the Fourier series fit ($k = 3$) for grid cells in the 90–100-km annulus. (e),(f) As in (c),(d), but with $k = 12$. (g),(h). As in (c),(d), but with $k = 24$. The small black plus signs indicate the location of the KGWX site and the red dots indicate flagged grid cells.

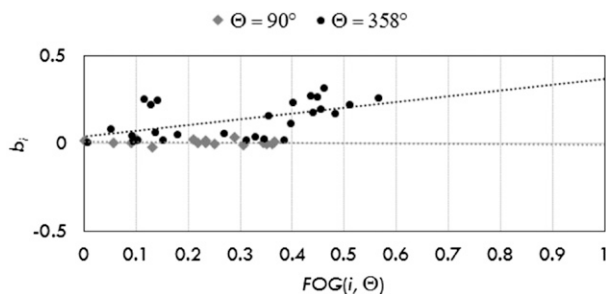


FIG. 5. Gridcell blocking strength b_i as a function of $FOG(i, \Theta)$ in two azimuthal sectors of the KGWX domain: $B(90^\circ) = -0.0064$ (◆) and $B(358^\circ) = 0.3677$ (●).

d. Determining blocking strength from flagged grid cells

After determining the individual gridcell blocking indicators, we look for radial consistency of nonzero b values in each azimuthal sector. Those suffering from beam blockage should have a substantial proportion of flagged ($b > 0$) to unflagged grid cells. However, simply counting the number of grid cells flagged in a given azimuthal sector (1° azimuthal sectors are denoted as Θ) is not an effective beam blockage criterion due to the complexities in the spatial relationship of the HRAP grid cells to azimuthal sectors. Some grid cells may lie entirely within an azimuthal sector, while others may encompass only a tiny corner and may be primarily affected by blocking presence or absence along a different azimuthal sector.

For each Θ , we determine the blocking strength using only grid cells with nonzero $FOG(\Theta)$ values. In an azimuthal sector with beam blockage, grid cells with the highest values of FOG (a metric that indicates the percentage overlap of the gridcell width with Θ) should systematically have positive values of b . We propose that the value of b when $FOG = 1$ should be the most direct measure of the extent to which beam blockage is affecting precipitation estimates within a azimuthal sector. However, very few grid points are completely within a single azimuthal sector (i.e., $FOG = 1$). Therefore, we need to use a function to determine the value of the blocking indicator when $FOG = 1$. We accomplish this by fitting a simple linear regression (SLR) to values of b as a function of FOG (e.g., Fig. 5).

In general, some grid cells in a blocked azimuthal sector will be unblocked, that is, will lie between the radar and an obstruction. Also, grid cells close to the radar will typically overlap many azimuthal sectors, making it unlikely that the effect of blocking would be linear as a function of FOG . To mitigate these issues, only grid cells greater than or equal to the median

distance from the radar site are used to compute the SLR fit at $FOG = 1$ in each azimuthal sector. Because of the polar coordinate geometry, this excludes only one-quarter of the area.

The SLR fit at $FOG = 1$ is designated as the azimuthal sector blocking strength B , with positive values indicative of beam blockage. The SLR fit for two azimuthal sectors (Fig. 5) at the KGWX radar shows a clear difference between those affected by beam blockage (e.g., 358°) and those unaffected (e.g., 90°).

Computing the blocking strength of each azimuthal sector is straightforward, but it does not determine whether actual beam blockage is present. The choice of an azimuthal sector blocking strength threshold value (B_0) that optimally identifies beam blockage while generally excluding cases of no beam blockage requires a trial and error examination of potential values. Ideally, a single threshold value such as 0.1 would adequately identify blockage of azimuthal sectors in all 102 radar coverage areas within the study domain. An azimuthal sector blocking strength value of 0.1 implies a 10% decrease in precipitation for grid cells completely within an azimuthal sector and is sufficient for many radar domains. This threshold was found to be appropriate for radars with noisier, or highly variable, precipitation distributions (e.g., Fig. 6a) but was found to be too high for radars with a smoother precipitation distribution (e.g., Fig. 6b). Noisiness is measured with a quantity called the mean absolute blocking strength \bar{B} , defined as

$$\bar{B} = \frac{1}{360^\circ} \sum_{\Theta=0^\circ}^{359^\circ} |B(\Theta)|. \tag{5}$$

The blocking strength threshold value B_0 in our algorithm is then

$$B_0 = \min(0.1, \bar{B}). \tag{6}$$

For reference, $\bar{B} = 0.25$ in the Jacksonville, Florida (KJAX) radar domain and $\bar{B} = 0.05$ in the North Platte, Nebraska (KLNK) radar domain.

e. Locating obstructions within azimuthal sectors

The last major step in the algorithm determines the distance from the radar site at which blockage initiates for azimuthal sectors whose values of B exceed the predetermined threshold. In general, obstacles may block more than one azimuthal sector simultaneously, so contiguously blocked azimuthal sectors are grouped together. Each such “multisector” $S(\Theta_1, \Theta_2)$ is treated as a single case of beam blockage (e.g., Fig. 7). If moving clockwise around an arc, multisector S is bounded by the

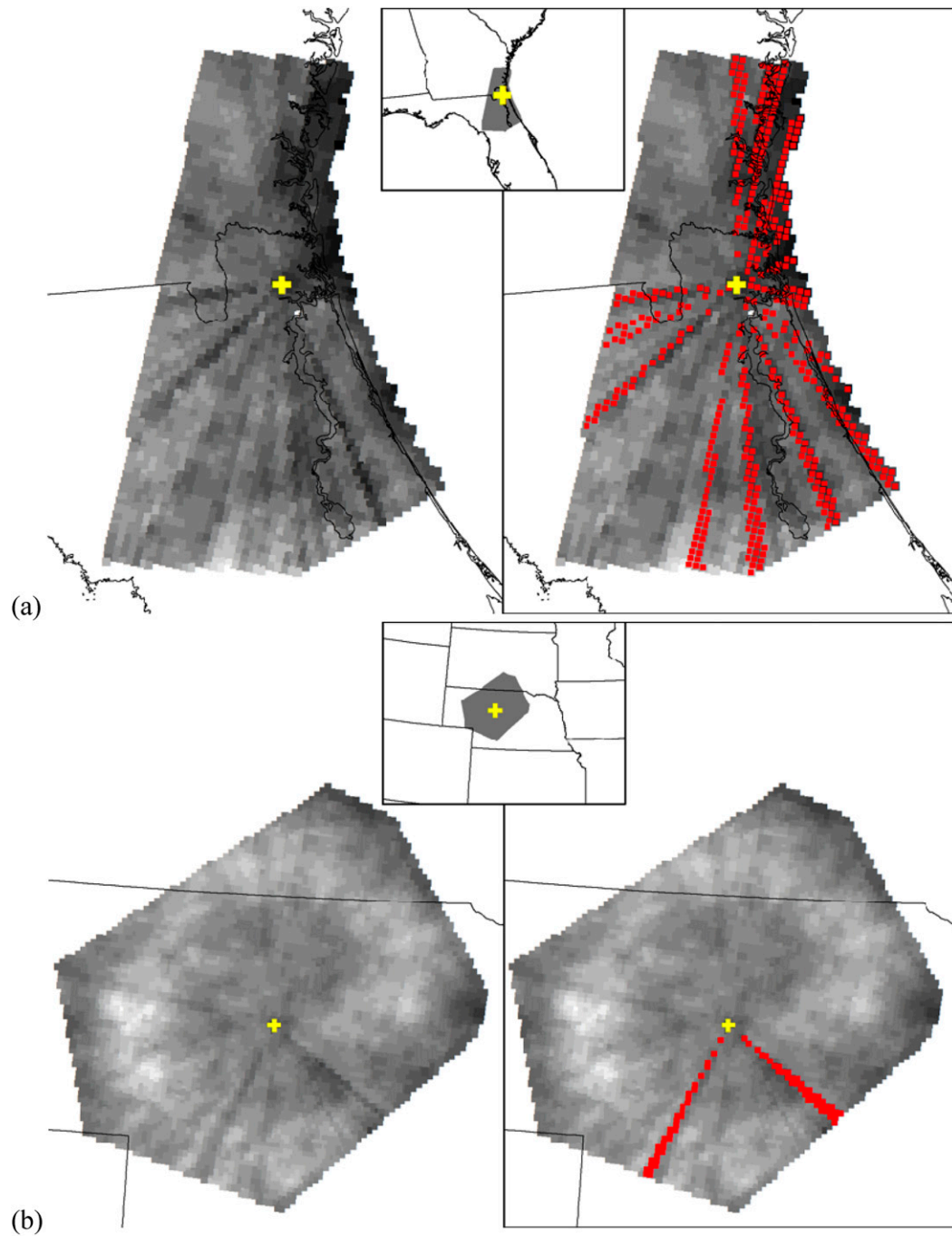


FIG. 6. Grid cells identified using $B_0 = 0.1$ in (a) KJAX and (b) KLNK radar domains.

left side of azimuthal sector Θ_1 and right side of azimuthal sector Θ_2 (where $\Theta_1 < \Theta_2$, unless S contains the 359° radial) with an azimuthal width $dS = \Theta_1 - \Theta_2 + 1$. Although the transmitted beam may intercept multiple fixed obstructions as it travels away from the radar site, the algorithm identifies a single dominant blockage distance within a multisector.

Each blocked S is partitioned into annulus sectors $S_A(d_1, d_2, \Theta_1, \Theta_2)$ using the same 10-km annuli as the Fourier series flagging (subscript A to denote being bounded by an annulus and to differentiate from the full multisector). This subsetting is done to find the distance of the obstruction d_B from the radar. For each annulus sector q , we determine an annular sector blocking

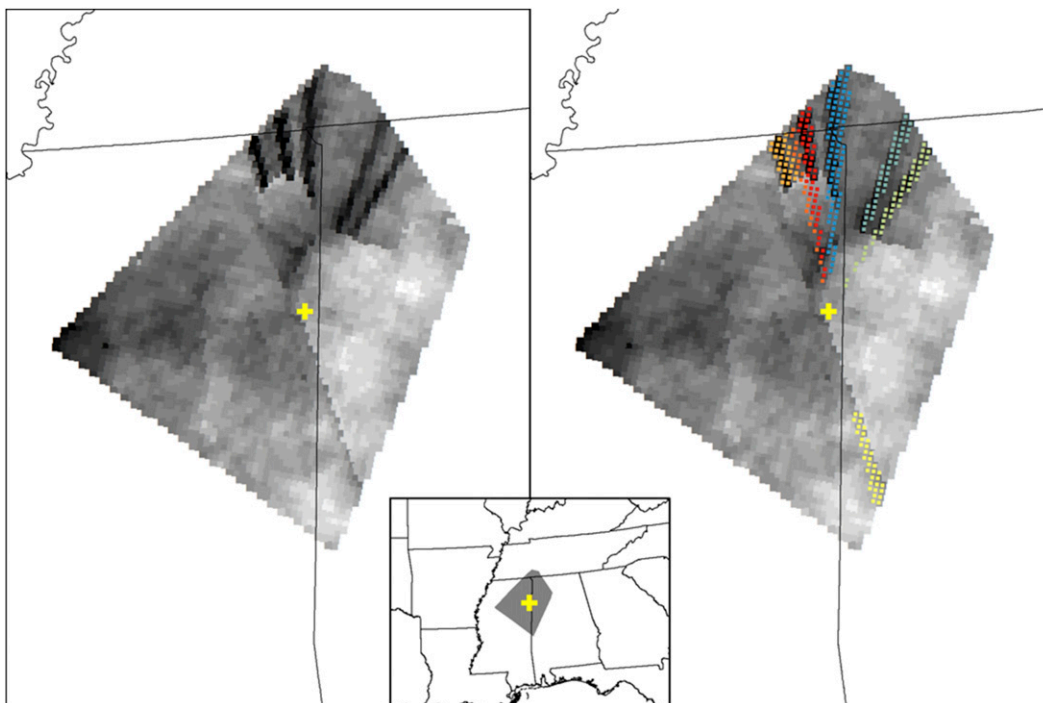


FIG. 7. Grid cells in azimuthal sectors (grouped by color) deemed blocked in the KGWX domain.

indicator $b_A(q)$ as a weighted average of all $n(q)$ overlapping grid cells, such that

$$b_A(q) = \frac{1}{n(q)} \sum_{i=1}^{n(q)} \text{FOG}(i) \times b(i). \quad (7)$$

It should be noted that the computation of $b_A(q)$ uses only grid cells within annulus sector q . Our conceptual model of blocking is a beam being fully or partially blocked by an obstruction and then affecting precipitation estimates at distances beyond the obstruction. Thus, if blockage begins at annulus sector x , then we should see consistently large values of b_A at farther distances than for annulus sectors closer to the radar site.

Therefore, we compute the annular sector blocking strength $B_A(q)$ as the median of all b_A values extending from q to the edge of the radar domain. Based on the vertical geometry of the radar beam (Rinehart 2004), any obstruction $d_B(S)$ should be within reasonable proximity to the radar site, that is, $d_B \leq d_{\max}$ (a predefined maximum distance from the radar for any potential obstructions). A d_{\max} value of 100 km was deemed to be an appropriate constraint for our study area. This is largely based on the long-range beam blockage signatures noticeable in the KGWX radar domain (Fig. 7). Constraining d_B eliminates false detection of beam blockage features at longer ranges, such

as the minimum in PNP at the western edge of the KGWX radar domain (Fig. 7).

For multisectors deemed to have blockage, a stepwise procedure determines which annular sector contains the beam blockage obstruction by using an “outside in” approach. The innermost annular sector $q(\Theta_1, \Theta_2)$ satisfying at least one of the following three sets of criteria is deemed to contain the obstruction:

- 1) $B_A(q) \geq B_0$ and $b_A(q) \geq B_0$. This is the most natural criterion.
- 2) $b_A(q) \geq B_0$, $n_A \geq 3$, and at least 75% of annulus sectors satisfy $b_A(q) \geq B_0/(\Theta_2 - \Theta_1 + 1)$, where n_A is the number of annulus sectors beyond q .
- 3) $B_A(q) \geq B_0/(\Theta_2 - \Theta_1 + 1)$ and $B_A(q)$ is greater than all B_A values in annulus sectors beyond q .

Whereas criterion 1 is intuitive, criteria 2 and 3 worked well for NWS QPEs within the testing period. Other metrics and/or thresholds may yield better results for different datasets. For criteria 2 and 3, the threshold B_0 is reduced as a factor of the number of azimuthal sectors contained in the multisector. In wider multisectors, partial blockage at the edges can reduce the overall annulus sector blocking strength value b_A , so a lower threshold is appropriate.

Azimuthal sectors initially designated as “blocked” in which no annular sectors meet any of the three criteria are changed to “unblocked” in the algorithm. For azimuthal sectors deemed blocked, d_B is narrowed down to the

innermost grid cell i within the annular sector chosen by the criteria above for which

$$\frac{b(i)}{\sum_{q=\Theta_1}^{\Theta_2} \text{FOG}(i, \Theta_q)} > \frac{B_0}{\Theta_2 - \Theta_1 + 1}. \quad (8)$$

The d_B is set as the distance of this innermost gridcell centroid d_i to the radar site. The beam blockage detection algorithm is complete upon determining the location of obstructions in each of the blocked azimuthal sectors (i.e., Fig. 7).

f. Temporal consistency of azimuthal sector blocking strength

The blockage detection algorithm was run for each possible 36-month period in the time frame of our study, January 2005–December 2012, for all 102 radars in our study domain. Our assumption is that because beam blockage is caused by a fixed obstruction, blocked azimuthal sectors should have a single B and a single distance of the obstruction from d_B for the entirety of the study period. Precipitation estimates, even aggregated over multiyear periods, have enough randomness to cause spurious blockage (and nonblockage) assessments. To minimize the impact of spurious assessments, we determined the median blocking strength value β (Θ) for each azimuthal sector over the entirety of the study period. For azimuthal sectors with a nonzero blocking strength, the distance of the obstacle from the radar $\delta_B(\Theta)$ is the median of the d_B values.

The assignment of a constant blocking strength is appropriate for most azimuthal sectors. However, there are exceptions in which the time series of blocking strengths shows a clear discontinuity between nonzero and zero (or vice versa) values (e.g., Fig. 8). We designed a simple test to identify the special cases in which the status of blocking changed within the study time frame, likely due to the growth or removal of trees and construction or demolition of buildings. A simple linear regression line was fit to the time series of azimuthal sector blocking strength values. If the slope m of the fit surpassed a threshold m_0 (e.g., Fig. 8), then the blocking status of the azimuthal sector was deemed to change at a single point in the time series. An appropriate value was found to be $m_0 = B_0 \div (n_{36} - 1)$, with n_{36} as the number of 36-month B values in the time series ($n_{36} = 61$ in our study).

Time series analysis is useful for identifying changes in blocking status, but the limited range of possible values $\{B = 0; B \geq B_0\}$ is not ideal for pinpointing a specific time for the change. A better metric to use is the departure of precipitation from an expected value (e.g., Fourier series fit), which has a continuous range of

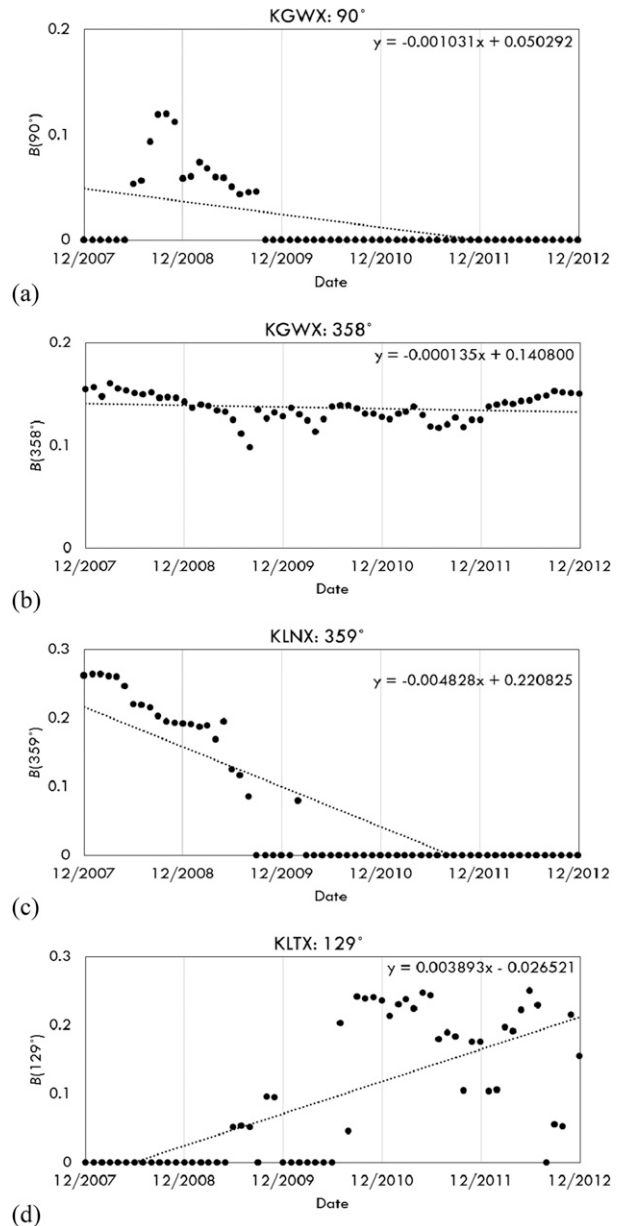


FIG. 8. Time series of the 36-month blocking strength values for (top to bottom) azimuthal sectors: KGWX 90° and 358°, and KLNKX 359° and 129°.

possible values. All azimuthal sectors with m exceeding the threshold m_0 signals a potential change in blocking. For these azimuthal sectors, the departure D (uppercase D to differentiate from distance to the radar d) is computed using all n grid cells with centroids lying both 1) within the azimuthal sectors and 2) beyond the median range of the azimuthal sector as

$$D(\Theta, t) = \sum_{i=1}^n \text{FOG}(i, \Theta) \times [\hat{P}(i, t) - P(i, t)]. \quad (9)$$

A positive departure in (7) indicates a lower-than-expected precipitation total.

For a blocked azimuthal sector, the distribution should be centered on a positive value with Gaussian-like variance. For azimuthal sectors with a change in blocking status, the expectation is for a transition from one distribution to the other over a length of time equal to the temporal resolution of the data, in our case 36 months. The beginning of this transition period is designated point t_B . For the case of blocking initializing (ceasing) at t_B , we expect the departure D to increase (decrease) during the transition period as a linear function of n , the number of months following the initialization of the blockage.

The transition period is found as the single period for which the two endpoints $D(\Theta, t_1)$ and $D(\Theta, t_2)$, where $t_1 < t_2$, have the largest absolute difference with the same sign as m_B . The candidate pairs used to determine the transition period are limited to the following (units are months):

- 1) Each pair where $t_2 - t_1 = 36$.
- 2) Each pair with $t_1 =$ December 2007 (first 36-month period in study) and $6 \leq t_2 - t_1 < 36$.
- 3) Each pair with $t_2 =$ December 2012 (last 36-month period in study) and $6 \leq t_2 - t_1 < 36$.

The last two criteria allow for identification of transition periods that cannot be fully encompassed by the time series of 36-month departures. If the transition period is identified using a pair of departure values meeting criterion 1 or 3, then the changepoint $t_B = t_1$. If the transition period is found using criterion 2, then the changepoint $t_B = t_2 - 36$ and is earlier than December 2007. In this study, the range of possible changepoints is July 2005–June 2012 (e.g., Fig. 9).

We then partition the time series of 36-month blocking strengths into discrete blocked, unblocked, and transition periods. For changepoints found using criterion 2 or 3, either the blocked or unblocked period is outside the footprint of the time series of $B(\Theta)$ values. If the blocked period is within the bounds of the time series, then the single azimuthal sector $\beta(\Theta)$ is found as the median of the values only within the blocked period. If the blocked period lies outside the time series, then a simple linear regression line is fit to the $B(\Theta)$ values in the transition period; the value of $\beta(\Theta)$ is the value of the fit where the line intersects the blocked period. The single azimuthal sector obstruction distance $\delta_B(\Theta)$ is found as the median of the d_B values from the algorithm transition period and the algorithm blocked period, if available.

g. Adjustment of precipitation for blocking

Once the blocked period is identified, any appropriate method for correcting for the blockage may be

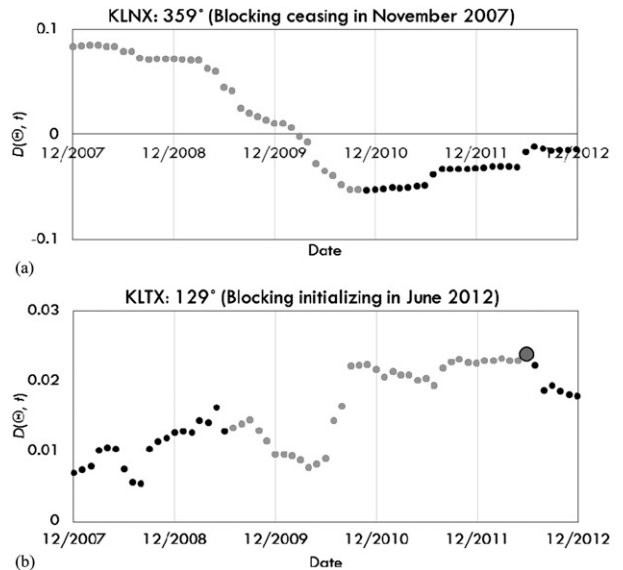


FIG. 9. Time series of the 36-month departures from the initial Fourier series fits for the azimuthal sectors in (a) Fig. 8c and (b) Fig. 8d. The gray circles indicate the transition period from blocking (no blocking) to no blocking (blocking) in (a) [(b)]. The large circle in (b) is the transition between nonblocking and blocking periods.

applied. In our algorithm, the basic methodology for adjusting precipitation estimates in grid cells affected by beam blockage is straightforward given the information collected by the detection algorithm. Our method lends itself better to making adjustments on shorter time scales (i.e., 1-month totals) and aggregating rather than adjusting the data at longer time scales and disaggregating.

In our study, we adjusted 1-month precipitation and aggregated to longer time scales. At each grid cell i and time t , we use the gridcell metric FOG and d in conjunction with the azimuthal sector metrics $\beta(\Theta)$ and δ_B to determine a beam blockage strength value B_{GC} at each grid cell:

$$B_{GC}(i, t) = \sum_{\Theta=0^\circ}^{359^\circ} w(\Theta, t) \times \begin{cases} 0, & \text{if } d(i) < \delta_B(\Theta) \\ \text{FOG}(i, \Theta) \times \beta(\Theta), & \text{if } d(i) \geq \delta_B(\Theta) \end{cases} \quad (10)$$

A weighting term $w = 1$ if azimuthal sector Θ is either always blocked or is considered blocked at time t , otherwise $w = 0$. The adjusted precipitation total $P_{ADJ}(i, t)$ is

$$P_{ADJ}(i, t) = \frac{P(i, t)}{1 - B_{GC}(i, t)} \quad (11)$$

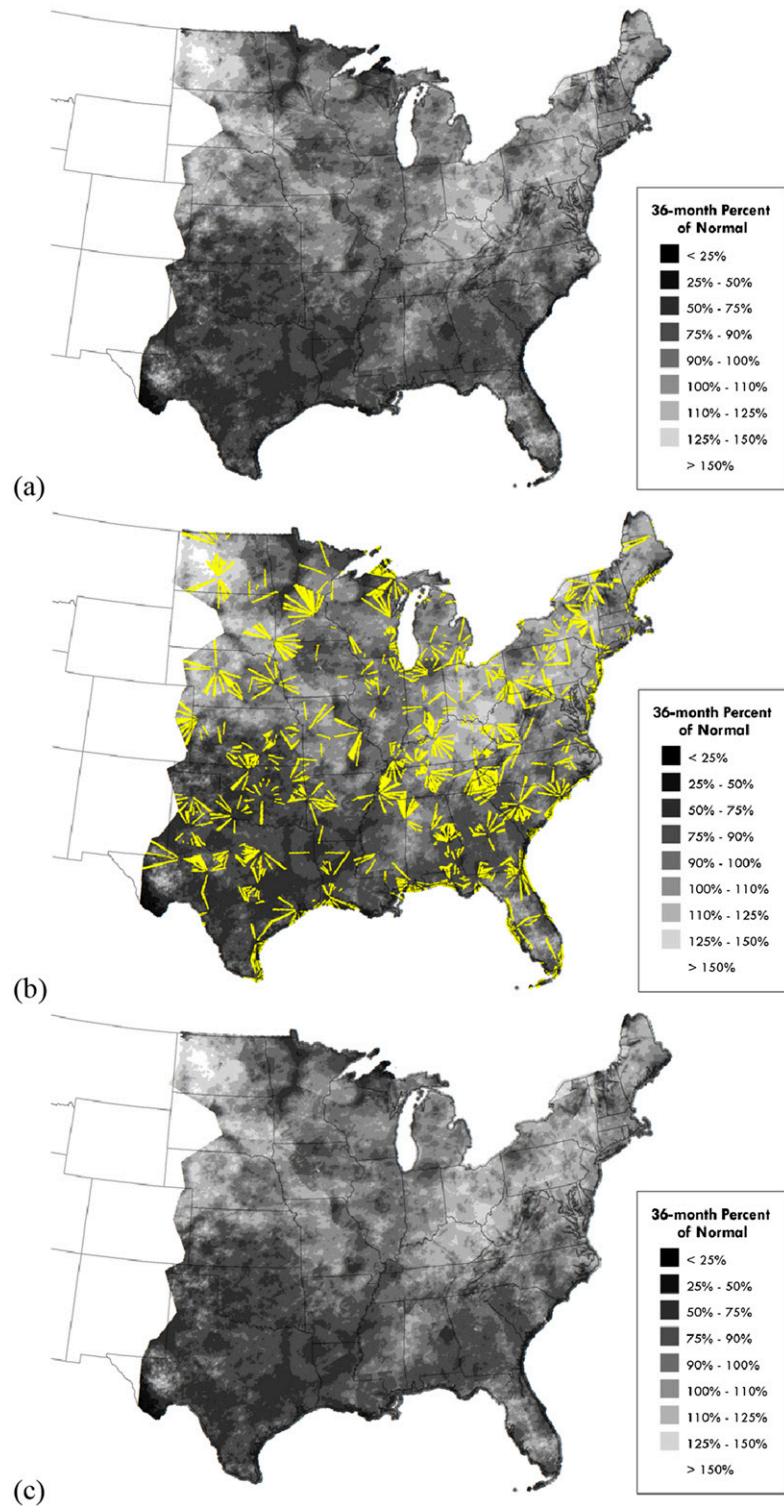


FIG. 10. (a) Original 36-month NWS QPE field 36-month ending 31 Dec 2012, (b) result of the beam blockage detection procedure, and (c) adjustment of P values for grid cells identified in the detection procedure.

TABLE 1. Overall underestimation bias for the blocked grid cells determined by the detection algorithm (actual), and average of the three rotated configurations (rotated) for different accumulation periods (months). Biases are computed for five thresholds of FOG_{GC} .

Period	FOG _{GC} threshold									
	≥10%		≥50%		≥75%		≥90%		100%	
	Actual	Rotated	Actual	Rotated	Actual	Rotated	Actual	Rotated	Actual	Rotated
All	0.067	0.012	0.095	0.021	0.110	0.025	0.120	0.027	0.122	0.030
1	0.027	-0.031	0.051	-0.031	0.070	-0.029	0.076	-0.028	0.070	-0.024
3	0.056	0.006	0.083	0.008	0.100	0.012	0.107	0.014	0.110	0.017
6	0.064	0.019	0.095	0.021	0.109	0.025	0.117	0.027	0.123	0.030
9	0.061	0.021	0.098	0.024	0.114	0.027	0.123	0.029	0.126	0.033
12	0.063	0.021	0.099	0.025	0.115	0.029	0.124	0.030	0.126	0.034
18	0.075	0.017	0.101	0.027	0.116	0.030	0.126	0.032	0.129	0.036
24	0.075	0.009	0.100	0.028	0.115	0.030	0.128	0.033	0.127	0.036
36	0.074	0.010	0.100	0.028	0.111	0.029	0.126	0.033	0.128	0.037

Figure 10 is a comparison of the original and adjusted precipitation fields for a sample 36-month period, which best illustrates the benefits of our methods.

4. Validation of beam blockage detection algorithm

a. Procedure

The beam blockage detection algorithm relies only on deciphering specific spatial properties of the radar precipitation estimates. This self-reliance means that gauge data, which were not used at all in either the beam blockage detection or the QPE adjustment, can be used as an independent data source to assess the validity of the algorithm. At each grid cell, the algorithm computed a time series of B_{GC} to assess the underestimation bias related to beam blockage, using the Fourier series analysis as a reference to do so. Where gauges are available, we can similarly assess the gauge-based underestimation bias using observational data through computing a quantity in the same manner as the blocking strength

$$B_G(i, t) = 1 - \frac{P(i, t)}{P_G(i, t)} \tag{12}$$

The goal of this validation exercise is to objectively determine whether the gauge-based underestimation bias computed in (12) is systematically larger within grid cells deemed blocked by the detection algorithm than those determined to be not blocked. A simple approach would be to divide the grid cells in each radar domain into a blocked group and an unblocked group and compute statistics on the underestimation bias in each group. However, radar underestimation of precipitation generally increases with distance from the radar site (Fabry et al. 1992; Smith et al. 1996; Seo et al. 2000). Given the spatial properties of beam blockage, the grid cells in the blocked group are systematically farther from the radar site, which would introduce a range-dependent bias into a comparison between the two groups.

A better approach will compare the underestimation bias of the blocked grid cells to grid cells with a similar distribution of d values. One method for doing so is to rotate the beam blockage detection field identified by

TABLE 2. Overall underestimation bias for the blocked grid cells determined by the detection algorithm (actual), and average of the three rotated configurations (rotated) for different accumulation periods (months). Biases are computed for four thresholds of B_{GC} .

Period	FOG _{GC} threshold							
	≥0.01		≥0.05		≥0.10		≥0.25	
	Actual	Rotated	Actual	Rotated	Actual	Rotated	Actual	Rotated
All	0.069	0.007	0.130	0.026	0.158	0.037	0.227	0.073
1	0.032	-0.032	0.088	-0.029	0.121	-0.020	0.205	-0.008
3	0.060	0.006	0.117	0.013	0.145	0.025	0.219	0.057
6	0.067	0.018	0.127	0.025	0.162	0.037	0.236	0.073
9	0.063	0.020	0.132	0.027	0.163	0.039	0.242	0.081
12	0.065	0.019	0.132	0.029	0.163	0.042	0.242	0.078
18	0.078	0.012	0.134	0.032	0.162	0.042	0.235	0.081
24	0.078	0.001	0.135	0.033	0.160	0.042	0.225	0.079
36	0.077	-0.004	0.138	0.034	0.162	0.043	0.200	0.089

the algorithm while keeping the PNP fields P and P_G fixed in space. We rotate the blockage field by 90° , 180° , and 270° to obtain three comparison configurations, respectively. For each rotation r , we compute the underestimation bias B_G of a control group of grid cells identified by the rotated blockage field. This method allows for a comparison of the beam-blockage-dependent underestimation bias to a similar subset of grid cells with the infiltration of range-dependent biases minimized.

b. Results of algorithm validation

Table 1 summarizes the results of the validation exercise for different thresholds of beam blockage (i.e., 100% represents total blockage), using gauges with no more than 10% of data missing. The fraction of the grid cell deemed blocked (FOG_{GC}) is computed as

$$\text{FOG}_{\text{GC}}(i, t) = \sum_{\theta=0^\circ}^{359^\circ} w_\theta(\Theta, t) \begin{cases} 0, & \text{if } d(i) < \delta_B(\Theta) \\ \text{FOG}(i, \Theta) \times \beta(\Theta), & \text{if } d(i) \geq \delta_B(\Theta) \end{cases} \quad (13)$$

The validation exercise confirmed the expectation that gauges located in grid cells identified as blocked by the algorithm should have a significantly larger gauge-based underestimation bias than those in the rotated blockage fields. Also, the underestimation bias increases as a function of the percentage of the grid cell blocked.

Table 2 is a similar table, comparing the underestimation bias for the actual configuration to the control groups, but is grouped by thresholds of B_{GC} . The underestimation bias increases as the blocking strength increases for both the actual and control groups, but the magnitude of the actual configuration is several times larger than the controls for all thresholds.

In addition, the original P estimates were compared to P_{ADJ} for grid cells with $\text{FOG} > 0$ and collocated with gauges (Table 3). The adjustment of the precipitation

TABLE 3. Average root-mean-square error (RMSE) for the P and P_{ADJ} estimates relative to gauges for grid cells identified with at least partial blockage ($\text{FOG}_{\text{GP}} > 0$). Data are categorized by the amount of blockage in the grid cells and represent all the accumulation periods in Tables 1 and 2. One square error value is computed as the difference between a gauge and radar (original and adjusted) PNP values.

FOG_{GC} (%)	Original RMSE	Adjusted RMSE	Change in RMSE (%)
<10	0.042	0.041	-1.1
10-20	0.030	0.028	-3.6
20-30	0.036	0.035	-3.5
30-40	0.032	0.030	-6.5
40-50	0.036	0.031	-12.6
50-60	0.032	0.028	-13.9
60-70	0.043	0.031	-27.5
70-80	0.032	0.026	-20.7
80-90	0.047	0.040	-16.0
90-100	0.056	0.039	-30.2
100	0.056	0.041	-27.4

was more effective as the value of FOG increased, around 30% for grid cells deemed at least 90% blocked. Additionally, the adjustment was more effective with an increase in accumulation period (see Table 4).

5. Discussion

This paper outlined an algorithm to objectively locate beam blockage features in gridded precipitation estimates. Beam blockage has been and will remain a challenging issue to deal with, even with advances in radar technology. There is no fundamental solution to improve the quality of reflectivity return in regions affected by beam blockage. Our solution compares the spatial patterns in long-term radar precipitation estimates with the expected geometry of beam blockage. An advantage to our approach over previous attempts is the

TABLE 4. As in Table 3, but with data categorized by the length of accumulation period (months).

Period	Original RMSE	Adjusted RMSE	Change in RMSE (%)
All	0.037	0.033	-10.9
1	0.113	0.110	-2.9
3	0.058	0.055	-6.1
6	0.041	0.037	-9.6
9	0.034	0.030	-11.7
12	0.031	0.027	-13.1
18	0.029	0.025	-14.3
24	0.026	0.022	-15.9
36	0.023	0.019	-17.8

minimal amount of real-time information that is required to run the algorithm. Once the radar and gridcell metadata information (including the gridded precipitation normals) is configured, the only real-time inputs to the algorithm are the gridded precipitation estimates.

The detection algorithm does not require any knowledge of the radar specifications or vertical characteristics (specific differential phase, specific attenuation, VPR, etc.); therefore, it is easily applicable to a number of different purposes. The algorithm can handle real-time datasets that are either radar-derived or multisensor datasets (i.e., the NWS QPEs) and is computationally inexpensive due to the relatively small amount of real-time input data.

The detection procedure can be run infrequently and still be effective. In fact, if one assumes the blocking obstructions to be fixed in time and space, then the algorithm needs to be run only a single time. However, there is quite a bit of manual intervention that went into the development of the algorithm, so usage for a different network may take several days of implementation. Tasks include obtaining all the relevant metadata and optimizing the different parameters corresponding to decision points in the algorithm. Relevant metadata needed are not only the coordinates of grid cells and radar sites but also the assignment of grid cells to radars and determining the distance, azimuth angle, and height of each grid cell to the nearest radar site.

If our algorithm for correcting the identified blocked grid cells is followed, then the corrections can be applied for precipitation totals on all time scales using a single value of blocking strength at each grid cell. There are alternatives for adjustment of the original precipitation value to account for beam blockage. One could compute the mean or median of a time series of blocking indicators at each grid cell and apply this to the entire time series of precipitation. Another method is to pick a single time—36-month (or shorter) period—at each grid cell as being representative of a single blockage indicator for the entire time series.

The primary focus of this paper was the detection of beam blockage rather than the adjustment of the precipitation totals. In the future, we plan to further investigate optimizing the use of the blocking indicator in adjusting precipitation estimates affected by beam blockage. Also, we will work to reduce the amount of manual adjustments in the current procedure, so that implementation in other systems is more straightforward and requires less manual intervention.

Acknowledgments. This study was funded by Award NA09NOS4780196 from the U.S. Department of Commerce's National Oceanic and Atmospheric Administration and Award 2011-67019-20042 from the U.S.

Department of Agriculture's National Institute of Food and Agriculture.

REFERENCES

- Andrieu, H., and J. D. Creutin, 1995: Identification of vertical profiles of radar reflectivity using an inverse method. Part I: Formulation. *J. Appl. Meteor.*, **34**, 225–239, doi:[10.1175/1520-0450\(1995\)034<0225:IOVPOR>2.0.CO;2](https://doi.org/10.1175/1520-0450(1995)034<0225:IOVPOR>2.0.CO;2).
- , —, G. Delrieu, and D. Faure, 1997: Use of a weather radar for the hydrology of a mountainous area. Part I: Radar measurement interpretation. *J. Hydrol.*, **193**, 1–25, doi:[10.1016/S0022-1694\(96\)03202-7](https://doi.org/10.1016/S0022-1694(96)03202-7).
- Bech, J., B. Codina, J. Lorente, and D. Bebbington, 2003: The sensitivity of single polarization weather radar beam blockage correction to variability in the vertical refractivity gradient. *J. Atmos. Oceanic Technol.*, **20**, 845–855, doi:[10.1175/1520-0426\(2003\)020<0845:TSOSPW>2.0.CO;2](https://doi.org/10.1175/1520-0426(2003)020<0845:TSOSPW>2.0.CO;2).
- Brandwood, D., 2012: *Fourier Transforms in Radar and Signal Processing*. 2nd ed. Artech House, 264 pp.
- Breidenbach, J. P., D.-J. Seo, P. Tilles, and K. Roy, 1999: Accounting for radar beam blockage patterns in radar-derived precipitation mosaics for River Forecast Centers. Preprints, *15th Conf. on Interactive Information and Processing Systems (IIPS)*, Dallas, TX, Amer. Meteor. Soc., 179–182.
- , —, —, and C. Pham, 2001: Seasonal variation in multi-radar coverage for WSR-88D precipitation estimation in a mountainous region. Preprints, *Conf. on Precipitation Extremes: Prediction, Impacts, and Responses*, Albuquerque, NM, Amer. Meteor. Soc., P2.38. [Available online at https://ams.confex.com/ams/annual2001/techprogram/paper_18668.htm.]
- Cifelli, R., W. A. Petersen, L. D. Carey, S. A. Rutledge, and M. A. F. Silva Dias, 2002: Radar observations of kinematic, microphysical, and precipitation characteristics of two MCSs in TRMM LBA. *J. Geophys. Res.*, **107**, 8077, doi:[10.1029/2000JD000264](https://doi.org/10.1029/2000JD000264).
- Daly, C., R. P. Neilson, and D. L. Phillips, 1994: A statistical-topographic model for mapping climatological precipitation over mountainous terrain. *J. Appl. Meteor.*, **33**, 140–158, doi:[10.1175/1520-0450\(1994\)033<0140:ASTMFM>2.0.CO;2](https://doi.org/10.1175/1520-0450(1994)033<0140:ASTMFM>2.0.CO;2).
- Diederich, M., A. Ryzhkov, C. Simmer, P. Zhang, and S. Troemel, 2015: Use of specific attenuation for rainfall measurement at X-band radar wavelengths. Part I: Radar calibration and partial beam blockage estimation. *J. Hydrometeorol.*, **16**, 487–502, doi:[10.1175/JHM-D-14-0066.1](https://doi.org/10.1175/JHM-D-14-0066.1).
- Fabry, F., G. L. Austin, and D. Tees, 1992: The accuracy of rainfall estimates by radar as a function of range. *Quart. J. Roy. Meteor. Soc.*, **118**, 435–453, doi:[10.1002/qj.49711850503](https://doi.org/10.1002/qj.49711850503).
- Friedrich, K., U. Germann, J. J. Gourley, and P. Tabary, 2007: Effects of radar beam shielding on rainfall estimation for the polarimetric C-band radar. *J. Atmos. Oceanic Technol.*, **24**, 1839–1859, doi:[10.1175/JTECH2085.1](https://doi.org/10.1175/JTECH2085.1).
- Fulton, R. A., 1998: WSR-88D polar to HRAP mapping. National Weather Service Office of Hydrology Hydrologic Research Laboratory Tech. Memo., 33 pp.
- , J. P. Breidenbach, D. Seo, D. A. Miller, and T. O'Bannon, 1998: The WSR-88D rainfall algorithm. *Wea. Forecasting*, **13**, 377–395, doi:[10.1175/1520-0434\(1998\)013<0377:TWRA>2.0.CO;2](https://doi.org/10.1175/1520-0434(1998)013<0377:TWRA>2.0.CO;2).
- Germann, U., G. Galli, M. Boscacci, and M. Bolliger, 2006: Radar precipitation measurement in a mountainous region. *Quart. J. Roy. Meteor. Soc.*, **132**, 1669–1692, doi:[10.1256/qj.05.190](https://doi.org/10.1256/qj.05.190).

- Istok, M. J., and Coauthors, 2009: WSR-88D dual polarization initial operational capabilities. *25th Conf. on Int. Interactive Information and Processing Systems (IIPS) for Meteorology, Oceanography, and Hydrology*, New Orleans, LA, Amer. Meteor. Soc., 15.5. [Available online at https://ams.confex.com/ams/89annual/techprogram/paper_148927.htm.]
- Joss, J., and A. Waldvogel, 1990: Precipitation measurement and hydrology. *Radar in Meteorology*, D. Atlas, Ed., Amer. Meteor. Soc., 577–600.
- , and R. Lee, 1995: The application of radar–gauge comparisons to operational precipitation profile corrections. *J. Appl. Meteor.*, **34**, 2612–2630, doi:10.1175/1520-0450(1995)034<2612:TAORCT>2.0.CO;2.
- Krajewski, W. F., A. Ntekos, and R. Goska, 2006: A GIS-based methodology for the assessment of weather radar beam blockage in mountainous regions: Two examples from the U.S. NEXRAD network. *Comput. Geosci.*, **32**, 283–302, doi:10.1016/j.cageo.2005.06.024.
- , G. Villarini, and J. A. Smith, 2010: Radar-rainfall uncertainties: Where are we after thirty years of effort? *Bull. Amer. Meteor. Soc.*, **91**, 87–94, doi:10.1175/2009BAMS2747.1.
- , B. Vignal, B.-C. Seo, and G. Villarini, 2011: Statistical model of the range-dependent error in radar–rainfall estimates due to the vertical profile of reflectivity. *J. Hydrol.*, **402**, 306–316, doi:10.1016/j.jhydrol.2011.03.024.
- Kucera, P. A., W. F. Krajewski, and C. B. Young, 2004: Radar beam occultation studies using GIS and DEM technology: An example study of Guam. *J. Atmos. Oceanic Technol.*, **21**, 995–1006, doi:10.1175/1520-0426(2004)021<0995:RBOSUG>2.0.CO;2.
- Lang, T. J., S. W. Nesbitt, and L. D. Carey, 2009: On the correction of partial beam blockage in polarimetric radar data. *J. Atmos. Oceanic Technol.*, **26**, 943–957, doi:10.1175/2008JTECHA1133.1.
- Lin, Y., and K. E. Mitchell, 2005: The NCEP stage II/IV hourly precipitation analyses: Development and applications. *19th Conf. on Hydrology*, San Diego, CA, Amer. Meteor. Soc., 1.2. [Available online at https://ams.confex.com/ams/Annual2005/techprogram/paper_83847.htm.]
- Rinehart, R. E., 2004: *Radar for Meteorologists*. 4th ed. Rinehart Publications, 482 pp.
- Ryzhkov, A., M. Diederich, P. Zhang, and C. Simmer, 2014: Potential utilization of specific attenuation for rainfall estimation, mitigation of partial beam blockage, and radar networking. *J. Atmos. Oceanic Technol.*, **31**, 599–619, doi:10.1175/JTECH-D-13-00038.1.
- Seo, D. J., J. P. Breidenbach, R. Fulton, D. Miller, and T. O’Bannon, 2000: Real-time adjustment of range-dependent biases in WSR-88D rainfall estimates due to nonuniform vertical profile of reflectivity. *J. Hydrometeorol.*, **1**, 222–240, doi:10.1175/1525-7541(2000)001<0222:RTAORD>2.0.CO;2.
- Smith, J. A., D. J. Seo, M. L. Baeck, and M. D. Hudlow, 1996: An intercomparison study of NEXRAD precipitation estimates. *Water Resour. Res.*, **32**, 2035–2045, doi:10.1029/96WR00270.
- Smith, P. L., 1998: On the minimum useful elevation angle for weather surveillance radar scans. *J. Atmos. Oceanic Technol.*, **15**, 841–843, doi:10.1175/1520-0426(1998)015<0841:OTMUEA>2.0.CO;2.
- Tabary, P., 2007: The new French operational radar rainfall product. Part I: Methodology. *Wea. Forecasting*, **22**, 393–408, doi:10.1175/WAF1004.1.
- Testik, F. Y., and M. Gebremichael, Eds., 2010: *Rainfall: State of the Science*. International Geophysics Series, Vol. 191, John Wiley & Sons, 287 pp.
- Vignal, B., and W. F. Krajewski, 2001: Large-sample evaluation of two methods to correct range-dependent error for WSR-88D rainfall estimates. *J. Hydrometeorol.*, **2**, 490–504, doi:10.1175/1525-7541(2001)002<0490:LSEO TM>2.0.CO;2.
- , H. Andrieu, and J. D. Creutin, 1999: Identification of vertical profiles of reflectivity from volume scan radar data. *J. Appl. Meteor.*, **38**, 1214–1228, doi:10.1175/1520-0450(1999)038<1214:IOVPOR>2.0.CO;2.
- Zhang, J., C. Langston, and K. Howard, 2008: Brightband identification based on vertical profiles of reflectivity from the WSR-88D. *J. Atmos. Oceanic Technol.*, **25**, 1859–1872, doi:10.1175/2008JTECHA1039.1.
- Zhang, P., D. Zrnić, and A. Ryzhkov, 2013: Partial beam blockage correction using polarimetric radar measurements. *J. Atmos. Oceanic Technol.*, **30**, 861–872, doi:10.1175/JTECH-D-12-00075.1.